Molecular Cell

Article

Structural basis of activation of the tumor suppressor protein neurofibromin

Graphical abstract

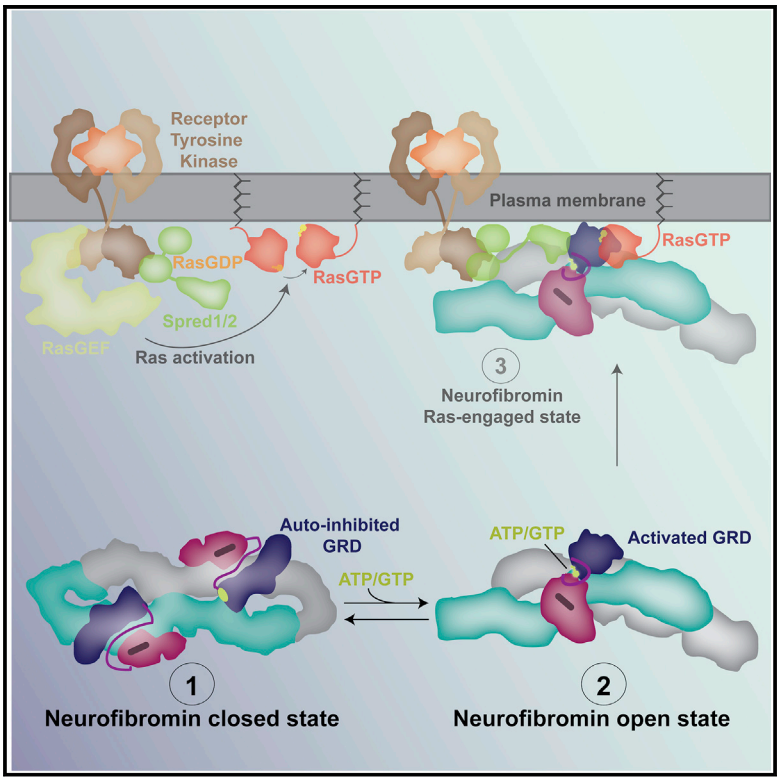

Highlights

- Neurofibromin exists in an equilibrium of occluded and open conformations
- Nucleotides allosterically activate neurofibromin by releasing auto-inhibition
- Open conformation of neurofibromin revealed by cryo-EM at 3.7 Å of resolution
- Disease-causing *NF1* mutations decrease neurofibromin stability and activity

Authors

Malik Chaker-Margot, Sebastiaan Werten, Theresia Dunzendorfer-Matt, Stefan Lechner, Angela Ruepp, Klaus Scheffzek, Timm Maier

Correspondence

klaus.scheffzek@i-med.ac.at (K.S.), timm.maier@unibas.ch (T.M.)

In brief

Neurofibromin, a GTPase-activating protein linked to the genetic disease neurofibromatosis type I, negatively regulates the small GTPase, Ras. Cryo-EM structures reveal neurofibromin in two conformations: an auto-inhibited occluded and an open, active state. Transition to the active conformation is stimulated by nucleotides, which release auto-inhibition.

Chaker-Margot et al., 2022, Molecular Cell *82*, 1288–1296
April 7, 2022
https://doi.org/10.1016/j.molcel.2022.03.011

CellPress

CellPress
OPEN ACCESS

Molecular Cell

Article

Structural basis of activation of the tumor suppressor protein neurofibromin

Malik Chaker-Margot,[1] Sebastiaan Werten,[2] Theresia Dunzendorfer-Matt,[2] Stefan Lechner,[2] Angela Ruepp,[2] Klaus Scheffzek,[2,*] and Timm Maier[1,3,*]

[1]Biozentrum, University of Basel, 4056 Basel, Switzerland
[2]Institute of Biological Chemistry, Biocenter, Medical University of Innsbruck, Innsbruck 6020, Austria
[3]Lead contact
*Correspondence: klaus.scheffzek@i-med.ac.at (K.S.), timm.maier@unibas.ch (T.M.)
https://doi.org/10.1016/j.molcel.2022.03.011

SUMMARY

Mutations in the *NF1* gene cause the familial genetic disease neurofibromatosis type I, as well as predisposition to cancer. The *NF1* gene product, neurofibromin, is a GTPase-activating protein and acts as a tumor suppressor by negatively regulating the small GTPase, Ras. However, structural insights into neurofibromin activation remain incompletely defined. Here, we provide cryoelectron microscopy (cryo-EM) structures that reveal an extended neurofibromin homodimer in two functional states: an auto-inhibited state with occluded Ras-binding site and an asymmetric open state with an exposed Ras-binding site. Mechanistically, the transition to the active conformation is stimulated by nucleotide binding, which releases a lock that tethers the catalytic domain to an extended helical repeat scaffold in the occluded state. Structure-guided mutational analysis supports functional relevance of allosteric control. Disease-causing mutations are mapped and primarily impact neurofibromin stability. Our findings suggest a role for nucleotides in neurofibromin regulation and may lead to therapeutic modulation of Ras signaling.

INTRODUCTION

Neurofibromatosis type 1 (NF1) is a familial syndrome associated with a predisposition to the formation of neurofibromas, benign and malignant tumors of the nervous system, pigmentation anomalies, bone deformations, and cognitive defects such as learning disabilities (Cichowski et al., 1999; Zhu et al, 2002). This autosomal dominant genetic disease is caused by mutations in the tumor suppressor gene *NF1*, which encodes the giant signaling protein neurofibromin (320 kDa) (Gutmann et al., 1991; Wallace et al., 1990). The *NF1* gene has also been found mutated in a large number of sporadic malignancies not associated with NF1 (Kiuru and Busam, 2017). Alterations to the *NF1* gene in patients include missense, nonsense, and frameshift mutations, splice site mutations, deletions, and insertions (Ko et al., 2013; Stenson et al., 2003). Neurofibromin, which is conserved across eukaryotes, acts as a GTPase-activating protein (GAP) to downregulate the activity of the small membrane-anchored guanine-nucleotide-binding protein Ras by accelerating its intrinsic rate of GTP hydrolysis and thereby modulates the Ras-MAPK and PI3K-Akt signaling pathways (Han et al., 1991; Martin et al., 1990). Ras itself is mutated in about 30% of human malignancies (Simanshu et al., 2017).

Neurofibromin contains two structurally characterized central domains, the GAP-related domain (GRD) and the phosphatidylinositol-transfer protein Sec14p-homologous domain and Pleckstrin-homology domain module, together referred to as Sec14-PH domain, flanked by extended predicted helical repeats (Figure 1A). The GRD not only carries out Ras GAP activity but also interacts via its GAP-extra domain (GAPex) with the EVH1 domain of SPRED proteins (Dunzendorfer-Matt et al., 2016; Stowe et al., 2012). SPRED proteins have been shown to mediate recruitment of neurofibromin to the plasma membrane via their C-terminal Sprouty domain (Dunzendorfer-Matt et al., 2016; Stowe et al., 2012). The Sec14-PH domain binds glycerophospholipids via its Sec14 module as well as phosphoinositide lipids, presumably via its PH domain (D'Angelo et al., 2006; Welti et al., 2007, 2011), which raises the possibility that lipid binding is directly involved in neurofibromin activation or membrane recruitment. The function of the flanking HEAT-like repeat domains is yet unknown, but single residue deletions or substitutions within these regions have been linked to *NF1*, suggesting an importance of the entire helical repeat scaffold for neurofibromin function (Ko et al., 2013). Beyond its role as a negative regulator of Ras, neurofibromin has also been implicated in other cellular functions, including the regulation of the adenylate-cyclase-protein kinase A (PKA) axis, although no mechanism has been proposed (Dasgupta et al., 2003; Guo et al., 1997; Ho et al., 2007).

While individual domains of neurofibromin have been crystalized (D'angelo et al., 2006; Scheffzek et al, 1998), the overall architecture of the protein has long remained elusive. Recently, structures of neurofibromin solved by cryoelectron microscopy (cryo-EM) have revealed the dimeric architecture of this protein, which rests in an equilibrium between two conformational states (Lupton et al., 2021; Naschberger et al., 2021), including an auto-inhibited closed conformation. However, the mechanism of

CellPress
OPEN ACCESS

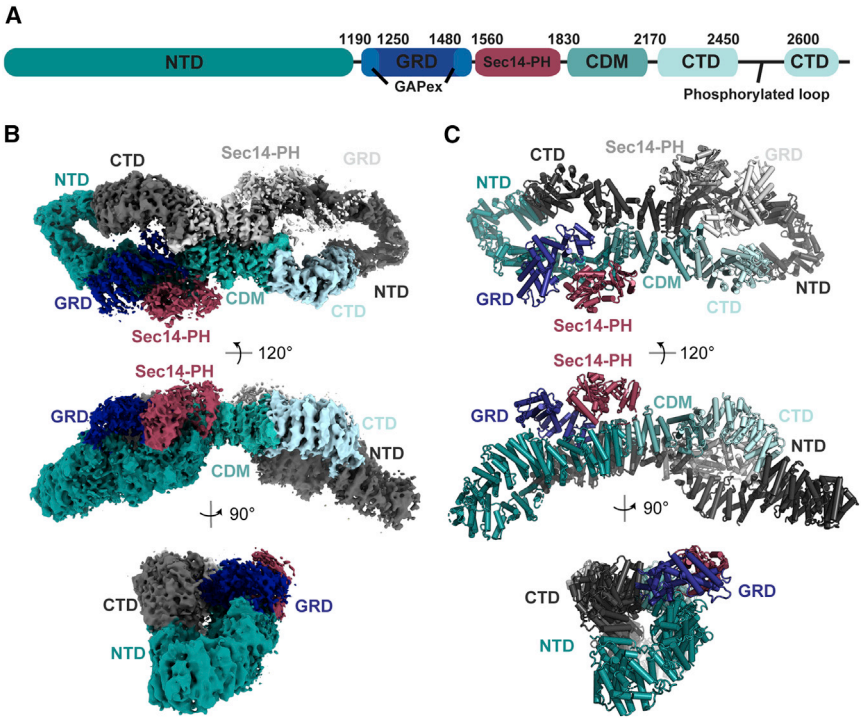

Figure 1. Human neurofibromin folds into an extended head-to-tail dimer

(A) Domain organization of neurofibromin: NTD (N-terminal domain, dark teal), GRD (GAP-related domain, dark blue), GAPex (GAP-extra domain, blue), Sec14-PH (secretory protein 14-pleckstrin homology-like module, raspberry), CDM (central dimerization module, teal), CTD (C-terminal domain, light blue), interrupted by a loop with reported phosphorylation sites.

(B) Cryo-EM reconstruction of neurofibromin in three different views. The domains of one protomer are colored as in (A), the second protomer is shown in shades of gray.

(C) Corresponding structural model of neurofibromin using the same color code as in (B).

neurofibromin activation remains unclear, impeded by lower resolution of the open-active conformation.

Here, we present cryo-EM structures of full-length human neurofibromin at approximately 3.7 Å resolution, in two distinct functional states, an occluded state, and a nucleotide-triggered open state. Together with a structure-guided biochemical characterization, these results reveal an unexpected layer of regulation for neurofibromin activity.

RESULTS

Neurofibromin forms a head-to-tail dimer with occluded Ras-binding site

Human neurofibromin (type I comprising 2,818 residues, UniProt: P21359-2) was recombinantly expressed in insect cells and purified as a 640 kDa homodimer based on size-exclusion chromatography with multi-angle light scattering detection (SEC-MALS) (Figure S1), consistent with previous work (Lupton et al., 2021; Sherekar et al., 2020). Purified neurofibromin was visualized by cryo-EM single particle analysis at an overall resolution of 3.7 Å (Figures S2 and S3). It adopts a figure eight shape of approximately 300 Å of diameter, formed by a large scaffold of alpha-helical repeats (Figures S4 and S5). Two domains per protomer protrude into the openings of the figure eight shape. They are visualized at lower local resolution presumably due to structural dynamics but can be unambiguously identified as the previously structurally characterized GRD and Sec14-PH domains (D'angelo et al., 2006; Scheffzek et al, 1998). For the same reason, lateral regions in the extended molecule are only resolved at lower resolution in the overall cryo-EM reconstruction. Local refinements enabled the improvement of resolution to 3.6 Å in the center, and local resolution of 4–5 Å in the extremities of the molecule (Figures 1B, 1C, S2, and S3; Data S1). An extended loop region between residues 2,450 and 2,600 that harbors a series of phosphorylation sites of unknown function (Dephoure et al., 2008; Zhou et al., 2013) remains unresolved (Figure S1).

Neurofibromin assembles as a natively domain-swapped head-to-tail dimer, with the two N-terminal helices (res. 1–50) forming contacts to helices on the C terminus (res. 2,632–2,669). In the center, helical regions from both protomers meet to provide the largest part of the dimer interface with an unusually large interface area of 3,750 Å^2. This central dimerization module (CDM) is built by homotypic interactions of extended helical repeat regions spanning from residue 1,830 to 2,160 in each protomer (Figures 1C, 2A, and S5), consistent with previous work (Lupton et al., 2021; Sherekar et al., 2020), and is well conserved only among metazoans implying that it evolved after they branched out (Figures S5 and S6).

The GRD is locked down into a crevice formed by the alpha-helical repeat scaffold by an interprotomer interaction, where the GAPex domain formed by residues flanking the GAP core (1,198–1,250 and 1,480–1,530), and in particular tyrosine 1,524 and its neighboring residues mediate contacts to residues 2,130–2,150 of the other protomer (Figure 2B). Strikingly, in this position the GRD-binding site for Ras is occluded by the surrounding CDM (Figure 2C), suggesting that the observed conformation of neurofibromin is not representing its active state. The GRD and its Ras-binding residues are exceptionally well conserved across metazoans and fungi (Figures S5 and S6). Notably, also the GAPex and its companion interacting residues 2,130–2,150 are similarly well conserved, especially across metazoans, supporting a conserved functional role.

Nucleotides induce an open state of neurofibromin with accessible Ras-binding sites

To get an understanding of the neurofibromin-Ras interaction, we obtained a cryo-EM reconstruction of neurofibromin in the presence of a molar excess of HRas loaded with the non-hydrolysable nucleotide GTP analog 5′-Guanylyl-imidodiphosphate (GMPPNP)

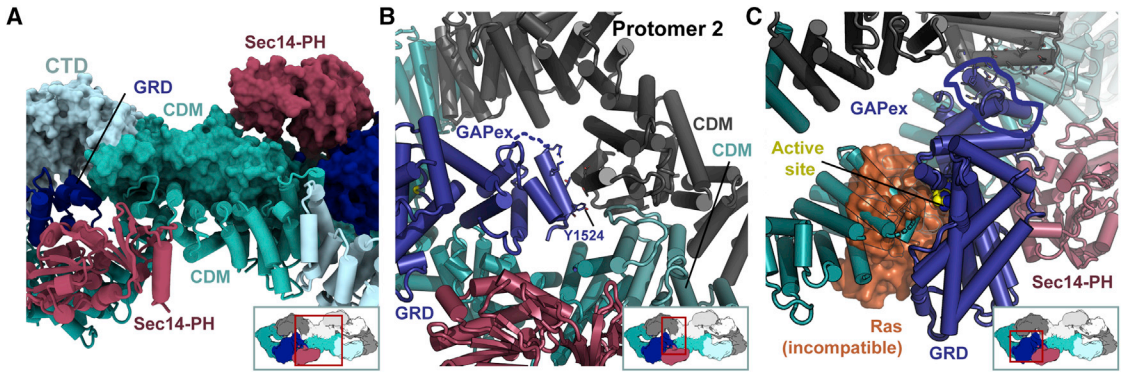

Figure 2. Occlusion of the Ras-binding site in neurofibromin

(A) Close-up view of the central part of the dimer interface formed by the CDM.

(B) Close-up view of the GAPex interprotomer contact tethering the GRD into the central scaffold cavity.

(C) Superposition of the GRD on our model, with the crystal structure of the GRD (dark blue) bound to KRas (orange) (PDB: 6OB2) demonstrates occlusion of the Ras-binding site by the neurofibromin scaffold.

and GTPγS at an overall resolution of 3.7 Å, which was improved with focused classification on one half of the molecule to 3.5 Å (Figures S2 and S3). The addition of both HRas:GMPPNP and GTPγS lead to a strikingly different asymmetric open conformation where the Sec14-PH domain of one protomer is rotated outwards and the corresponding GRD is placed above a central groove in the CDM core (Figures 3A–3D; Video S1; Data S1), while the GRD-Sec14-PH region of the second protomer is pushed outwards and remains highly flexible. In addition, we also resolved a possible intermediate conformation wherein one of the GRDs still occupied its locked-down position while the other swings out and is flexibly linked (Figure S2) to a resolution of 3.5 Å, providing the highest quality representation of the entire helical scaffold region (Figure S3). Surprisingly, by collecting cryo-EM datasets where only nucleotides were added to wild-type neurofibromin in the absence of HRas, we observed based on 2D class averaging that the open conformation can be induced solely by the addition of either GTPγS or ATP at a concentration of 10 mM (Figure S7). Importantly, that conformation has not been observed in multiple data collection for neurofibromin in the absence of added nucleotide.

This raises the question of how the addition of nucleotides may induce the opening of neurofibromin. In the open conformation, the contact between the GAPex domain around residues Y1524 and H1530 and the helical scaffold that locks down the entire GRD is lost. The GRD undergoes a massive 116° rotation relative to the neighboring Sec14-PH domain, with the GAPex together with the linker between Sec14-PH now forming an interface linking Sec14-PH and GRD (Figure 3C). Unexpectedly, within this new interface we observed additional density that we interpret as bound nucleotide (Figures 3F, 3G, S8A, and S8B), with the guanylyl base stacked between the aromatic side chains of Y1524 and W1538 and the negatively charged phosphate chain surrounded by the basic groups of R1207, R1513, K1517 in the GRD, and K1547 located in the GRD-Sec14 linker. Despite the possible formation of hydrogen bonds, no strict structural mechanism for ensuring base specificity is observed. Strikingly, the set of residues involved in nucleotide binding in the open conformation, namely Y1524 and K1517, overlaps with the residues that form the interprotomer contact locking down the GRD to the scaffold in the occluded form of neurofibromin (Figures 3F, 3G, and S3I). This dual residue function provides a direct rationalization of the triggering mechanism for nucleotide ligand induced conformational change. Presumably, as a result of the released GRD-scaffold interaction and the new GRD-Sec14 interface, the Sec14-PH domain rotates outward with the GRD and the overall bend of the helical scaffold no longer holding the GRD is relaxed. In the final open conformation, the Sec14-PH-GRD domains of one protomer are orderly bound by a network of interactions between residues of the GRD and the central groove of the CDM formed by both protomers. This interaction breaks the overall dimer symmetry and leaves no equivalent binding site for the second protomer's GRD region, which remains flexibly linked, although weak density is still observed in a new position (Figure 3B; Data S1). Superimposing the Ras-bound GRD structure onto the ordered GRD in the open neurofibromin suggest steric compatibility with Ras binding, as the CDM would neatly accommodate Ras with the GRD located above it (Figure 3E). The other, more flexible GRD would similarly be able to interact with Ras in this conformation, meaning that both domains may be active.

Notably, HRas was not visualized in our cryo-EM reconstruction of the open state, suggesting that its binding to the ordered GRD is either weak or transient under our experimental conditions, as has been seen before for GAPs (Su et al., 2021) or that it preferentially associates with the flexibly attached GRD-Sec14-PH region.

The closed conformation represents an auto-inhibited state

To confirm and quantify nucleotide binding by the neurofibromin GRD-Sec14-PH segment, we determined dissociation constants for adenosine and guanosine di- and triphosphates by isothermal titration calorimetry (ITC). Binding was observed for all nucleotides with K_D values ranging from 5 to 15 mM

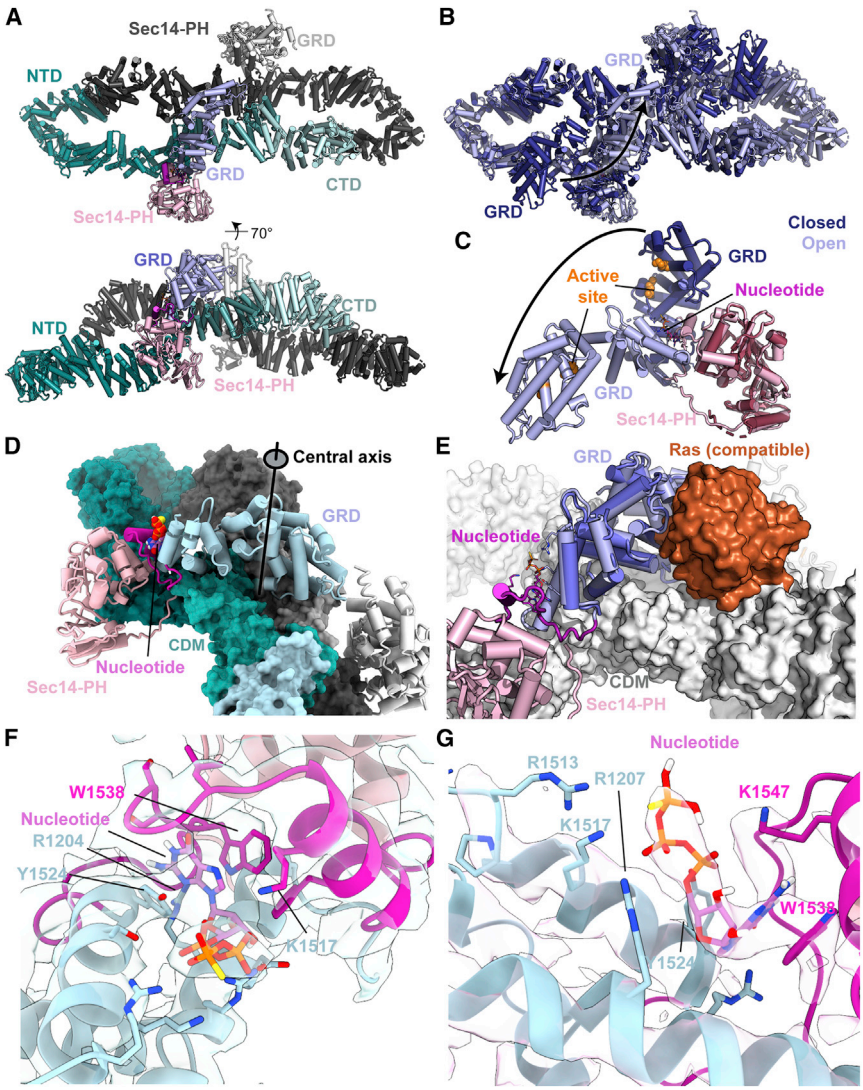

Figure 3. The nucleotide-induced open conformation of neurofibromin

(A) Orthogonal views of the open conformation of neurofibromin in cartoon representation, colored as in Figure 1A, but using lighter shades for GRD and Sec14-PH to distinguish open and occluded state.

(B) Superimposition of the occluded and open conformations showing the shift in the GRD position.

(C) Overlay of the GRD-Sec14-PH module in the occluded and open conformation, showing the 116° rotation of the GRD relative to the Sec14-PH domain.

(D) Cartoon representation of the GRD located above the central groove of the CDM.

(E) Superimposition of the KRas-bound GRD crystal structure (PDB: 6OB2) on the open conformation model, showing little to no clashes with the helical scaffold.

(F) Model and experimental map for the modeled nucleotide recognition site focusing on the nucleotide base.

(G) As in (F), but focusing on the nucleotide phosphates.

(Figures 4E and S8). Given that ATP is the only nucleotide that would reach such cellular concentrations, varying from 0.5 to 10 mM (Dragon et al., 1998; Gribble et al., 2000; Larcombe-McDouall et al., 1999; Traut, 1994), this would, intriguingly, suggest an effect of ATP concentration on neurofibromin activity in cells, although we cannot rule out that the effects of local concentration, production, and degradation of nucleotides may dominate whole-cell concentration estimations.

Our structural analysis suggests a dual role of the GAPex domain, with overlapping binding sites around residue Y1524, it forms scaffold interactions in the occluded state and binds nucleotides in the open state. To test the functional relevance of these interactions, we employed HPLC-based RasGAP activity assays where neurofibromin shows substantial turnover of GTP (Figure 4C). Introduction of two-point mutations, substituting the aromatic residues Y1524 and W1538 in the nucleotide-binding site for alanine, enhances the enzymatic activity significantly, presumably by weakening the GAPex-scaffold interaction and shifting the equilibrium to the open state. In comparison, the isolated GRD shows the highest activity (Figure 4C). At the same time, these mutations lead to approximately 5-fold reduction in nucleotide affinity, indicating that nucleotide binding is not a critical component for the intrinsic activity of the GRD, but serves primarily to release the lockdown of the GAPex domain in the occluded state (Figures 4E and S8). A mutant variant of neurofibromin designed to form disulfide bridges across the GAPex-scaffold interface (Figures 4A and 4B) by replacing two residues on each side for cysteines (Cys-Cys mutant, L1520C, Y1524C, T2133C, and E2134C), is almost completely inactive, but pre-incubation with 10 mM dithiothreitol to reduce disulfide bonds restores activity to wild-type levels (Figure 4D). This suggests first that a state with the GAPex domain locked down to the scaffold is fully inactive, in agreement with the incompatibility of Ras binding, and second, that neurofibromin in the absence of activating ligands is in a conformational equilibrium of occluded and open state.

We addressed the impact of nucleotides on the conformational equilibrium of neurofibromin by activity measurements (Figure 4F). Assays were performed at low GTP concentration (200 μM), which based on the estimated K_D (~5 mM), leaves neurofibromin in its occluded conformation. Upon addition of ATP (2 mM), we observe an approximately 60% increase in GAP activity, confirming that high concentrations of ATP shift the equilibrium to the active state. Data obtained using the Y1524/W1538A mutant defective in nucleotide binding reveal no change in activity upon ATP addition, as expected. These results suggest that the ATP-induced open conformation of

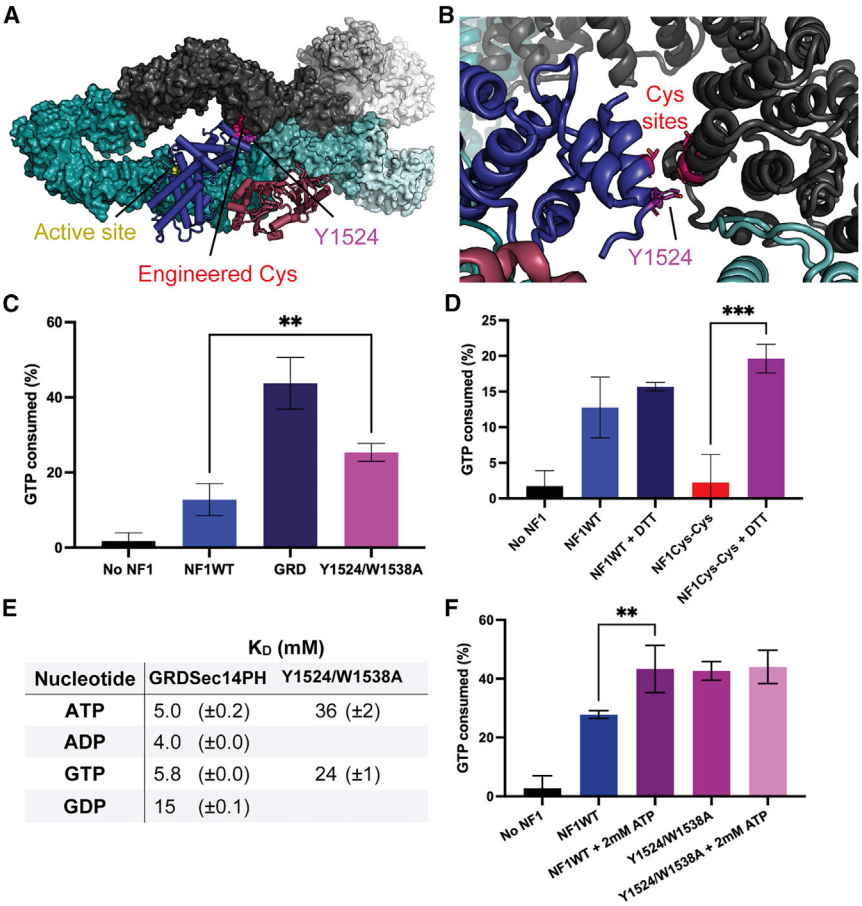

E

	K_D (mM)	
Nucleotide	GRDSec14PH	Y1524/W1538A
ATP	5.0 (±0.2)	36 (±2)
ADP	4.0 (±0.0)	
GTP	5.8 (±0.0)	24 (±1)
GDP	15 (±0.1)	

Figure 4. The GAPex domain controls neurofibromin activation via nucleotide binding

(A) Overview of the neurofibromin engineered mutants' sites relative to the active site for Y1524A, L1520C, Y1524C, T2133C, and E2134C.

(B) Close-up view of mutated residues as shown in (A).

(C) GAP assays measuring the change in GTP turnover by HRas in presence or absence of neurofibromin wild-type, in the presence of the neurofibromin GRD domain, and a double alanine mutant of neurofibromin. Error bars represent SD, n = 3–6, **p < 0.01.

(D) GAP assays as in (C) for neurofibromin wild-type and the Cys-Cys mutant in the presence or absence of DTT, error bars represent SD, n = 3–6, ***p < 0.001.

(E) Binding affinity of the GRD-Sec14-PH domains (encompassing the entire nucleotide binding site) for selected nucleotides. Listed K_D values were determined by isothermal titration calorimetry (ITC) for the wild-type and Y1524/W1538A variant.

(F) GAP assays comparing the activity of wild-type and Y1524/W1538A neurofibromin in the presence of 2 mM of ATP, error bars represent SD, n = 6, **p < 0.01.

neurofibromin is similar to the engineered neurofibromin variant (Y1524/W1538A) defective in interprotomer contact and in nucleotide binding.

The GAP-extra domain also acts as the binding site for SPRED proteins via their EVH1 domain (Dunzendorfer-Matt et al., 2016). Superimposing the structure of the EVH1-GRD onto both the occluded and open conformation of neurofibromin, demonstrates that EVH1 domain docking is fully permitted by both conformations, suggesting that SPRED1 binding would not impact catalysis, in agreement with earlier reports (Figure S9) (Dunzendorfer-Matt et al., 2016). Indeed, we did not observe any significant differences in activity of neurofibromin in the presence or the absence of the SPRED1-EVH1 domain (Figure S9D). Thus, the primary role for SPRED1 interaction also in the context of neurofibromin is apparently membrane recruitment.

Disease-related mutations affect stability and activity of neurofibromin

The structure of neurofibromin in two states allows us to rationalize the effect of non-truncating missense mutations associated with *NF1*. Pathogenic mutations include large deletions which either remove the catalytic domain or lead to an unstable gene product (Amberger et al., 2015; Stenson et al., 2003), but also more than 1,500 missense mutations affecting 868 residues in neurofibromin (Figure 5) based on the OMIM and Human Gene Mutation Database (HGMD) databases (Amberger et al., 2015; Stenson et al., 2003). Disease-causing mutations of neurofibromin are dispersed throughout the protein, not only clustered in the GRD (Figures 5A and 5B), suggesting that the physiological function of the Sec14-PH and GRD domains requires the extended helical scaffold, for example, for regulating activity or for serving as binding sites for additional protein partners (Wang et al., 2011; Xie et al., 2016). Disease-related point mutations are underrepresented in the CDM, possibly because this large interaction surface might be resilient to single point mutations (Figure 5C).

We set out to gain more insights into the effects of prominent disease-causing mutations by determining the GAP activity as well as the stability of the mutated neurofibromin variants (Figures 5D and 5E). All variants showed reduced GAP activity (Figure 5E). Mutants located in the GRD (R1276E, K1423E) abolished GAP activity without reducing protein stability. The mutation R1809G in the PH domain, one of the most commonly mutated positions in neurofibromin (Figure 5C), has no negative impact on stability and causes only a modest reduction in GAP activity, suggesting that this mutation rather has an indirect effect on protein-protein interactions or membrane association. Mutations in the helical scaffold surrounding the GRD (dM991, P1084R, R1849Q, and L2076P) impact stability (not analyzed for W777R) and activity ranging from 10% reduction in activity for the R1849Q mutant, to completely abolishing activity for the W777R mutation, presumably by a negative impact on the ability to form a stable open conformation of neurofibromin. The mutation G1869S in a loop of the CDM is noteworthy

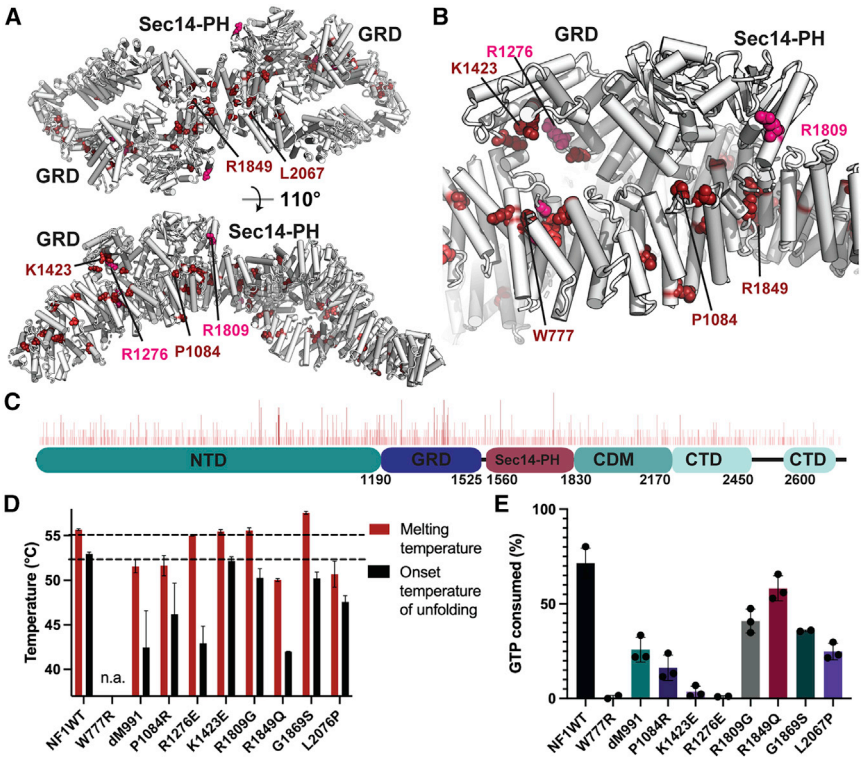

Figure 5. Mapping the disease-associated mutations of neurofibromin

(A) Cartoon representation of neurofibromin with positions of mutations colored in shades of red, with mutants used in this work highlighted. Residues affected by more than two mutations are displayed as spheres.

(B) Close-up view of the GRD and Sec14-PH domain, and the adjacent helical repeats.

(C) Domain organization diagram of neurofibromin superposed with a histogram of disease-causing mutations per residue position.

(D) Differential scanning fluorimetry assay of neurofibromin in its wild-type form (NF1 WT) and eight variants carrying the indicated missense mutations (n = 3). Melting and onset of unfolding temperatures are shown in red and black respectively; errors bars denote SD.

(E) Ras GAP assays of the same neurofibromin mutants, showing that disease-causing mutants display lower activity than wild type (n = 3).

because it causes an approximately 80% reduction of activity without a negative impact on neurofibromin stability. This position is surface exposed without any proximity to functional domains in the occluded state, not providing any clue to an effect on GAP activity. However, in the open conformation, this loop is located directly in the docking site for the GRD, suggesting that the mutation to serine impairs the ability to form a stable open neurofibromin conformation (Figure S10).

DISCUSSION

Small guanine-nucleotide-binding proteins have long been known to control cellular signaling, metabolism, and dynamics. More recently, several studies have highlighted the complex regulation of GAP and GEF proteins, which control GTPase activity. In both GAPs, such as the Rheb-GAP tuberous sclerosis complex (TSC) (Yang et al., 2021) or the ArfGAP C9ORF72 (Su et al., 2021), and GEFs, like the Rac-GEF DOCK2-ELMO1 (Chang et al., 2020), the GTPase-regulating domain is embedded into extended helical repeat scaffolds. These scaffolds serve to regulate and locate GAP/GEF activity with metabolites, signaling molecules or other proteins, based on interactions that are highly specific to their respective system. Neurofibromin has been studied for decades due to its critical role as a GAP for Ras, one of the most commonly mutated proteins in cancer, and due to its direct link to the familial genetic disease NF1. Still, the functional role of the majority of neurofibromin and potential mechanisms for controlling its GAP activity remained enigmatic.

We propose a model in which neurofibromin exists in an equilibrium between an active open conformation, and a closed inactive state (Figure 6). Binding of a nucleotide shifts the equilibrium toward the active state. With the help of SPRED proteins and/or lipid-mediated interactions, neurofibromin is recruited to the membrane where it stimulates GTPase activity in the membrane-tethered Ras (Figure 6).

The transition between these states starts with breaking an interface between the helical scaffold and the GAPex domain. Intramolecular interactions of GAPex domains in GAP proteins have not been visualized before, but, notably, the GAPex domain in the Rac1-GAP IQGAP2 has been implicated in autoinhibitory intramolecular interactions with the protein's C-terminal region (Ozdemir et al., 2018). This interface is apparently stabilized by binding of nucleotides, suggesting a physiological cross talk between energy and nucleotide state of a cell and Ras signaling, although we cannot exclude that other ligands with related properties may also stimulate neurofibromin *in vivo*. ATP is the only nucleotide whose estimated whole-cell concentration are high enough to possibly bind neurofibromin based on the affinity measured here (Dragon et al., 1998; Gribble et al., 2000; Larcombe-McDouall et al., 1999; Traut, 1994). Notably, ATP concentrations have been shown to vary in response to cellular activity, such as muscle contraction or an action potential, which could theoretically lead to neurofibromin inhibition (Trevisiol et al., 2017). While the influence of nucleotides on the conformational state of neurofibromin was unexpected, such finding is not unprecedented in Ras-MAP kinase signaling: ATP has recently been identified as a negative regulator of B-Raf kinase domain oligomerization and activity, thereby inhibiting Ras-MAPK signaling, consistent with our results (Liau et al., 2020). While this is somewhat counterintuitive, it could point toward a mechanism by which high ATP concentrations are sensed in a negative feedback loop to maintain homeostasis.

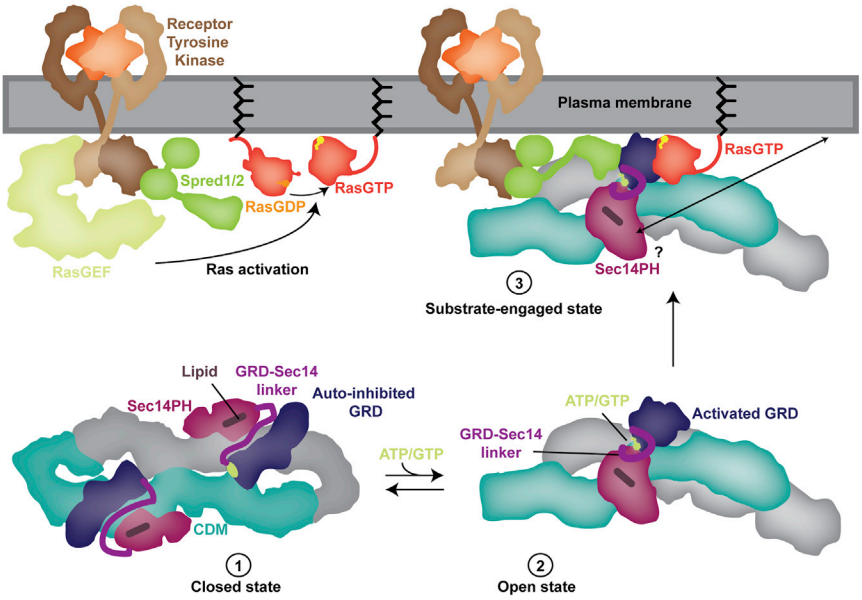

Figure 6. Model of neurofibromin activation

Diagram showing the conformational equilibrium of neurofibromin, controlled by nucleotide binding, and its recruitment of neurofibromin to the plasma membrane by SPRED1/2, where it engages with its substrate Ras. Possible interactions between phosphoinositides and the Sec14-PH domain may also contribute to neurofibromin recruitment or retention at the cell membrane.

Ras has been postulated to act as a dimer (Güldenhaupt et al., 2012). Although our data do not prove or disprove whether Ras signals as a monomer or dimer, it is notable that models of Ras homodimers can be superimposed without clash onto the open conformation of neurofibromin. Specifically, our model allows for the possibility that the two neurofibromin GRDs may interact simultaneously with two sets of Ras homodimers, but likely not a single homodimer. While the occluded conformation is incompetent for Ras binding, both states of neurofibromin are compatible with the interaction of the SPRED-EVH1 domain, which mediates membrane recruitment of neurofibromin via interacting with the GAPex domain (Figure 6). The interaction of the Sec14-PH domain with membranes and lipids may also impact the transition between occluded and open conformation. Notably, in the cryo-EM structure of the open conformation with better local resolution of the Sec14-PH domain, residual density is observed in the previously reported lipid-binding pocket, demonstrating that lipid interaction is compatible with the open state of neurofibromin. However, the positions of the PH domains in the open conformation are such that it is unlikely for both to be able to interact with the membrane simultaneously, given that they are oriented in opposite directions, in contrast to the occluded conformation. The scaffold region may be involved in further regulatory protein-protein interactions, such as the p97-neurofibromin complex formation (Wang et al., 2011).

A recent paper reported the structure of neurofibromin in a closed and semi-open conformation, which shows good agreement between our model and theirs (Naschberger et al., 2021). The authors of Naschberger et al. report a zinc-ion-binding site composed of Cys1032, His1558, and His1576 and a water molecule (using isoform II numbering, UniProt: P21359-1), which they claim stabilizes the protein into the closed conformation. In our maps, the resolution surrounding this putative zinc-binding site is too low in the closed conformation to confirm the presence of a metal ion. Crucially, the corresponding histidines (H1537 and H1555) involved in this proposed interaction are located near the nucleotide-binding site in our open conformation model, suggesting that if both regulatory models are true, the zinc ion would have to be stripped out before the GRD-Sec14PH linker may be rearranged into a conformation compatible with nucleotide binding.

The present visualization and functional analysis of two functional states of neurofibromin provides a critical basis for understanding the impact of the numerous disease-related *NF1* mutations, as well as further protein-protein crosstalk. In particular, the lack of clear explanation for why the very common R1809G mutation would impair neurofibromin function implies a Ras-independent mechanism and deserves further investigation. The identification of novel interfaces controlling conformational activation opens new paths for specific small-molecule-based intervention to enhance or inhibit neurofibromin activity and Ras signaling, which may prove relevant for future treatments of familial NF1 and cancers.

Limitations of the study

Due to our results being derived exclusively from *in vitro* experiments, the exact nature of neurofibromin regulation *in vivo* remains unclear. Notably, the interplay between nucleotide levels, zinc signaling, and other small molecule or protein interactors of neurofibromin on its activity will have to be elucidated in a cellular or organism context.

STAR★METHODS

Detailed methods are provided in the online version of this paper and include the following:

- KEY RESOURCES TABLE
- RESOURCE AVAILABILITY
  - Lead contact
  - Materials availability
  - Data and code availability
- EXPERIMENTAL MODEL AND SUBJECT DETAILS
- METHOD DETAILS
  - Construct for recombinant expression of neurofibromin
  - Protein expression and purification for structural analysis
  - Protein production for activity assays

- Cryo-EM sample preparation and collection
- Cryo-EM data processing
- Structural modeling and visualization
- HPLC-based Ras GAP assay
- SEC-MALS
- Mass spectrometry analysis
- Isothermal titration calorimetry
- Thermal stability measurement

● QUANTIFICATION AND STATISTICAL ANALYSIS

SUPPLEMENTAL INFORMATION

Supplemental information can be found online at https://doi.org/10.1016/j.molcel.2022.03.011.

ACKNOWLEDGMENTS

We thank Mohamed Chami and Lubomir Kovacik from the Biozentrum BioEM lab for assistance with operating the microscopes and the sciCORE scientific computing facility for computer and software support. Timothy Sharpe assisted with MALS and ITC data acquisition and analysis, and Ulrike Lanner provided support for the mass spectrometry analysis. We would like to thank Jeanette Seiler, Fabien Bonneau, Annabel Parret, Imre Berger, and Darren Hart for support in construct/protein expression design and setup of the initial protein production system; and Barbara Fuernrohr, Giridhar Shivalingaiah, and Clara Baldin for support in protein production. We also thank Nikolaus Pfanner and Anne Spang for critical comments on the manuscript and Rob Russell for discussion. Timm Maier is supported by the Swiss National Science Foundation (SNF) projects 179323 and SNF R'Equip 177084. Klaus Scheffzek is supported by the Austrian Science Fund (FWF): 28975. Malik Chaker-Margot is supported by Human Frontiers Research Project (HFSP) long-term fellowship LT000121/2019-L. Sebastiaan Werten was supported by an EMBO Scientific Exchange Grant.

AUTHOR CONTRIBUTIONS

M.C.-M. expressed and purified the proteins for activity assays, prepared and analyzed cryo-EM samples, analyzed cryo-EM data, and performed structural modeling and activity assays. S.L. designed and prepared constructs and protocols for protein used in cryo-EM. S.W., T.D.-M., and A.R. expressed the protein for cryo-EM collection and biochemical characterization. K.S., T.M., and M.C.-M. planned and designed experiments. M.C.-M., K.S., and T.M. wrote the manuscript, and all authors edited this manuscript.

DECLARATION OF INTERESTS

The authors declare no competing interests.

Received: November 15, 2021
Revised: January 14, 2022
Accepted: March 3, 2022
Published: March 29, 2022

REFERENCES

Adams, P.D., Afonine, P.V., Bunkóczi, G., Chen, V.B., Davis, I.W., Echols, N., Headd, J.J., Hung, L.W., Kapral, G.J., Grosse-Kunstleve, R.W., et al. (2010). PHENIX: a comprehensive Python-based system for macromolecular structure solution. Acta Crystallogr. D Biol. Crystallogr. *66*, 213–221.

Amberger, J.S., Bocchini, C.A., Schiettecatte, F., Scott, A.F., and Hamosh, A. (2015). OMIM.org: Online Mendelian Inheritance in Man (OMIM®), an online catalog of human genes and genetic disorders. Nucleic Acids Res. *43*, D789–D798.

Chang, Leifu, Yang, Jing, Jo, Chang Hwa, Boland, Andreas, Zhang, Ziguo, McLaughlin, Stephen H, Abu-Thuraia, Afnan, Killoran, Ryan C, Smith, Matthew J, Côté, Jean-Francois, and Barford, David (2020). Structure of the DOCK2-ELMO1 complex provides insights into regulation of the autoinhibited state. Nat Commun *11* (1), 3464. https://doi.org/10.1038/s41467-020-17271-9.

Cichowski, K., Shih, T.S., Schmitt, E., Santiago, S., Reilly, K., McLaughlin, M.E., Bronson, R.T., and Jacks, T. (1999). Mouse models of tumor development in neurofibromatosis type 1. Science *286*, 2172–2176.

D'Angelo, I., Welti, S., Bonneau, F., and Scheffzek, K. (2006). A novel bipartite phospholipid-binding module in the neurofibromatosis type 1 protein. EMBO Rep. *7*, 174–179.

Dasgupta, B., Dugan, L.L., and Gutmann, D.H. (2003). The neurofibromatosis 1 gene product neurofibromin regulates pituitary adenylate cyclase-activating polypeptide-mediated signaling in astrocytes. J. Neurosci. *23*, 8949–8954.

Dephoure, N., Zhou, C., Villén, J., Beausoleil, S.A., Bakalarski, C.E., Elledge, S.J., and Gygi, S.P. (2008). A quantitative atlas of mitotic phosphorylation. Proc. Natl. Acad. Sci. USA *105*, 10762–10767.

Dragon, S., Hille, R., Götz, R., and Baumann, R. (1998). Adenosine 3′:5′-cyclic monophosphate (cAMP)-inducible pyrimidine 5′-nucleotidase and pyrimidine nucleotide metabolism of chick embryonic erythrocytes. Blood *91*, 3052–3058.

Dunzendorfer-Matt, T., Mercado, E.L., Maly, K., McCormick, F., and Scheffzek, K. (2016). The neurofibromin recruitment factor Spred1 binds to the GAP related domain without affecting Ras inactivation. Proc. Natl. Acad. Sci. USA *113*, 7497–7502.

Emsley, P., and Cowtan, K. (2004). Coot: model-building tools for molecular graphics. Acta Crystallogr. D Biol. Crystallogr. *60*, 2126–2132.

Goddard, T.D., Huang, C.C., Meng, E.C., Pettersen, E.F., Couch, G.S., Morris, J.H., and Ferrin, T.E. (2018). UCSF ChimeraX: meeting modern challenges in visualization and analysis. Protein Sci. *27*, 14–25.

Gribble, F.M., Loussouarn, G., Tucker, S.J., Zhao, C., Nichols, C.G., and Ashcroft, F.M. (2000). A novel method for measurement of submembrane ATP concentration. J. Biol. Chem. *275*, 30046–30049.

Güldenhaupt, J., Rudack, T., Bachler, P., Mann, D., Triola, G., Waldmann, H., Kötting, C., and Gerwert, K. (2012). N-Ras forms dimers at POPC membranes. Biophys. J. *103*, 1585–1593.

Guo, H.-F., The, I., Hannan, F., Bernards, A., and Zhong, Y. (1997). Requirement of *Drosophila* NF1 for activation of adenylyl cyclase by PACAP38-like neuropeptides. Science *276*, 795–798.

Gutmann, D.H., Wood, D.L., and Collins, F.S. (1991). Identification of the neurofibromatosis type 1 gene product. Proc. Natl. Acad. Sci. USA *88*, 9658–9662.

Han, J.W., McCormick, F., and Macara, I.G. (1991). Regulation of Ras-GAP and the neurofibromatosis-1 gene product by eicosanoids. Science *252*, 576–579.

Ho, I.S., Hannan, F., Guo, H.-F., Hakker, I., and Zhong, Y. (2007). Distinct functional domains of neurofibromatosis type 1 regulate immediate versus long-term memory formation. J. Neurosci. *27*, 6852–6857.

Jumper, J., Evans, R., Pritzel, A., Green, T., Figurnov, M., Ronneberger, O., Tunyasuvunakool, K., Bates, R., Žídek, A., Potapenko, A., et al. (2021). Highly accurate protein structure prediction with AlphaFold. Nature *596*, 583–589.

Kiuru, M., and Busam, K.J. (2017). The NF1 gene in tumor syndromes and melanoma. Lab. Invest. *97*, 146–157.

Ko, J.M., Sohn, Y.B., Jeong, S.Y., Kim, H.-J., and Messiaen, L.M. (2013). Mutation spectrum of NF1 and clinical characteristics in 78 Korean patients with neurofibromatosis type 1. Pediatr. Neurol. *48*, 447–453.

Larcombe-McDouall, J., Buttell, N., Harrison, N., and Wray, S. (1999). *In vivo* pH and metabolite changes during a single contraction in rat uterine smooth muscle. J. Physiol. *518*, 783–790.

Liau, N.P.D., Wendorff, T.J., Quinn, J.G., Steffek, M., Phung, W., Liu, P., Tang, J., Irudayanathan, F.J., Izadi, S., Shaw, A.S., et al. (2020). Negative regulation of RAF kinase activity by ATP is overcome by 14-3-3-induced dimerization. Nat. Struct. Mol. Biol. *27*, 134–141.

Lupton, C.J., Bayly-Jones, C., D'Andrea, L., Huang, C., Schittenhelm, R.B., Venugopal, H., Whisstock, J.C., Halls, M.L., and Ellisdon, A.M. (2021). The cryo-EM structure of the human neurofibromin dimer reveals the molecular basis for neurofibromatosis type 1. Nat. Struct. Mol. Biol. *28*, 982–988.

Martin, G.A., Viskochil, D., Bollag, G., McCabe, P.C., Crosier, W.J., Haubruck, H., Conroy, L., Clark, R., O'Connell, P., and Cawthon, R.M. (1990). The GAP-related domain of the neurofibromatosis type 1 gene product interacts with ras p21. Cell *63*, 843–849.

Naschberger, A., Baradaran, R., Rupp, B., and Carroni, M. (2021). The structure of neurofibromin isoform 2 reveals different functional states. Nature *599*, 315–319.

Ozdemir, E.S., Jang, H., Gursoy, A., Keskin, O., Li, Z., Sacks, D.B., and Nussinov, R. (2018). Unraveling the molecular mechanism of interactions of the Rho GTPases Cdc42 and Rac1 with the scaffolding protein IQGAP2. J. Biol. Chem. *293*, 3685–3699.

Pettersen, E.F., Goddard, T.D., Huang, C.C., Couch, G.S., Greenblatt, D.M., Meng, E.C., and Ferrin, T.E. (2004). UCSF Chimera—a visualization system for exploratory research and analysis. J. Comput. Chem. *25*, 1605–1612.

Punjani, A., Rubinstein, J.L., Fleet, D.J., and Brubaker, M.A. (2017). cryoSPARC: algorithms for rapid unsupervised cryo-EM structure determination. Nat. Methods *14*, 290–296.

Punjani, A., Zhang, H., and Fleet, D.J. (2020). Non-uniform refinement: adaptive regularization improves single-particle cryo-EM reconstruction. Nat. Methods *17*, 1214–1221.

Scheffzek, K., Ahmadian, M.R., Wiesmüller, L., Kabsch, W., Stege, P., Schmitz, F., and Wittinghofer, A. (1998). Structural analysis of the GAP-related domain from neurofibromin and its implications. EMBO J. *17*, 4313–4327.

Sherekar, M., Han, S.-W., Ghirlando, R., Messing, S., Drew, M., Rabara, D., Waybright, T., Juneja, P., O'Neill, H., Stanley, C.B., et al. (2020). Biochemical and structural analyses reveal that the tumor suppressor neurofibromin (NF1) forms a high-affinity dimer. J. Biol. Chem. *295*, 1105–1119.

Simanshu, D.K., Nissley, D.V., and McCormick, F. (2017). RAS proteins and their regulators in human disease. Cell *170*, 17–33.

Stenson, P.D., Ball, E.V., Mort, M., Phillips, A.D., Shiel, J.A., Thomas, N.S.T., Abeysinghe, S., Krawczak, M., and Cooper, D.N. (2003). Human Gene Mutation Database (HGMD®): 2003 update. Hum. Mutat. *21*, 577–581.

Stowe, I.B., Mercado, E.L., Stowe, T.R., Bell, E.L., Oses-Prieto, J.A., Hernández, H., Burlingame, A.L., and McCormick, F. (2012). A shared molecular mechanism underlies the human rasopathies Legius syndrome and neurofibromatosis-1. Genes Dev. *26*, 1421–1426.

Su, M.-Y., Fromm, S.A., Remis, J., Toso, D.B., and Hurley, J.H. (2021). Structural basis for the ARF GAP activity and specificity of the C9orf72 complex. Nat. Commun. *12*, 3786.

Traut, T.W. (1994). Physiological concentrations of purines and pyrimidines. Mol. Cell. Biochem. *140*, 1–22.

Trevisiol, A., Saab, A.S., Winkler, U., Marx, G., Imamura, H., Möbius, W., Kusch, K., Nave, K.-A., and Hirrlinger, J. (2017). Monitoring ATP dynamics in electrically active white matter tracts. eLife *6*, e24241.

Wallace, M.R., Marchuk, D.A., Andersen, L.B., Letcher, R., Odeh, H.M., Saulino, A.M., Fountain, J.W., Brereton, A., Nicholson, J., and Mitchell, A.L. (1990). Type 1 neurofibromatosis gene: identification of a large transcript disrupted in three NF1 patients. Science *249*, 181–186.

Wang, H.-F., Shih, Y.-T., Chen, C.-Y., Chao, H.-W., Lee, M.-J., and Hsueh, Y.-P. (2011). Valosin-containing protein and neurofibromin interact to regulate dendritic spine density. J. Clin. Invest. *121*, 4820–4837.

Welti, S., Fraterman, S., D'Angelo, I., Wilm, M., and Scheffzek, K. (2007). The Sec14 homology module of neurofibromin binds cellular glycerophospholipids: mass spectrometry and structure of a lipid complex. J. Mol. Biol. *366*, 551–562.

Welti, S., Kühn, S., D'Angelo, I., Brügger, B., Kaufmann, D., and Scheffzek, K. (2011). Structural and biochemical consequences of NF1 associated nontruncating mutations in the Sec14-PH module of neurofibromin. Hum. Mutat. *32*, 191–197.

Xie, K., Colgan, L.A., Dao, M.T., Muntean, B.S., Sutton, L.P., Orlandi, C., Boye, S.L., Boye, S.E., Shih, C.-C., Li, Y., et al. (2016). NF1 is a direct G protein effector essential for opioid signaling to Ras in the striatum. Curr. Biol. *26*, 2992–3003.

Yang, H., Yu, Z., Chen, X., Li, J., Li, N., Cheng, J., Gao, N., Yuan, H.-X., Ye, D., Guan, K.-L., and Xu, Y. (2021). Structural insights into TSC complex assembly and GAP activity on Rheb. Nat. Commun. *12*, 339.

Zhou, H., Di Palma, S., Preisinger, C., Peng, M., Polat, A.N., Heck, A.J.R., and Mohammed, S. (2013). Toward a comprehensive characterization of a human cancer cell phosphoproteome. J. Proteome Res. *12*, 260–271.

Zhu, Y., Ghosh, P., Charnay, P., Burns, D.K., and Parada, L.F. (2002). Neurofibromas in NF1: Schwann cell origin and role of tumor environment. Science *296*, 920–922.

STAR★METHODS

KEY RESOURCES TABLE

REAGENT or RESOURCE	SOURCE	IDENTIFIER
Bacterial and virus strains		
E. Coli NEB® 10-beta	New England Biolabs	Cat: C3019H
E. Coli DH10MultiBac	Geneva Biotech	DH10MultiBac
E. Coli BL21(DE3)	New England Biolabs	Cat: C2527H
Chemicals, peptides, and recombinant proteins		
GTP	Jena Bioscience	Cat: NU-1012
GTPγS	Jena Bioscience	Cat: NU-412
ATP	Jena Bioscience	Cat: NU-1010
ADP	Jena Bioscience	Cat: NU-1198
GMPPNP	Jena Bioscience	Cat: NU-899
cAMP	Jena Bioscience	Cat: NU-1503S
DTT	Goldbio	Cat: DTT10
Gateway™ BP Clonase™ II Enzyme mix	Thermo Fisher	Cat: 11789100
Gateway™ LR Clonase™ II Enzyme mix	Thermo Fisher	Cat: 11791020
DYKDDDDK peptide	Genscript	Cat: RP10586
Trypsin Protease (Lysyl endopeptidase)	Fujifilm Wako Chemical	Cat: 121-05063
Glu-C Protease, Sequencing Grade	Promega	Cat: V165A
Deposited data		
Structure of neurofibromin occluded conformation	This work	PDB: 7R03
EM maps for neurofibromin occluded conformation	This work	EMDB: EMD-14218
Structure of neurofibromin open conformation	This work	PDB: 7R04
EM maps for neurofibromin open conformation	This work	EMDB: EMD-14219
Raw SDS-PAGE gels for Figure S1.	This work	Mendeley Data: https://doi.org/10.17632/wk39ssk7ct.1
Experimental models: Cell lines		
SF21 Insect cells	Expression Systems	Cat: 94-010F
Oligonucleotides		
GGGGACAAGTTTGTACAAAAAAGCAG GCTTAGAGAATCTGTATTTCCAGGGG atggaggagcagatgaggctgcc	This work	AttB1-TEV-Sos1-564-F
GGGGACCACTTTGTACAAGAAAGCTG GGTTTCAggtacctggtcttgggtttgatgg	This work	AttB2-Sos1-1049R
GGGGACAAGTTTGTACAAAAAAGCAG GCTTAGAGAATCTGTATTTCCAGGGG actgaattcgacaccctggcc	This work	attB1_TEV_NF1co_1191F
GGGGACCACTTTGTACAAGAAAGCTG GGTTTCActctggaggacccaggtatgcaag	This work	attB2_NF1_1528
GGGGACCACTTTGTACAAGAAAGCTG GGTTTCAggagtcgggctgtgacagc	This work	attB2_NF1co_1817R
Recombinant DNA		
synNF1 wild-type	This work	N/A
synNF1 W777R	This work	N/A
synNF1 dM991	This work	N/A
synNF1 P1084R	This work	N/A
synNF1 R1276Q	This work	N/A

(*Continued on next page*)

Continued

REAGENT or RESOURCE	SOURCE	IDENTIFIER
synNF1 K1423E	This work	N/A
synNF1 R1809G	This work	N/A
synNF1 R1849Q	This work	N/A
synNF1 G1869V	This work	N/A
synNF1 L2067P	This work	N/A
Software and algorithms		
cryoSPARC v2	Punjani et al., 2020	https://cryosparc.com/
Coot 0.9.4	Emsley and Cowtan, 2004	https://www2.mrc-lmb.cam.ac.uk/personal/pemsley/coot
PyMol 2.4.2	Schrödinger LLC	https://pymol.org
PHENIX 1.19	Adams et al., 2010	https://www.phenix-online.org/documentation/index.html
UCSF Chimera	Pettersen et al., 2004	https://www.cgl.ucsf.edu/chimera/
UCSF ChimeraX	Goddard et al., 2018	https://www.cgl.ucsf.edu/chimerax
Prism 9	GraphPad Software, Inc	https://www.graphpad.com/scientific-software/prism/
Other		
Quantifoil R2/1 200 Mesh	Electron Microscopy Sciences	Cat: Q210CR1

RESOURCE AVAILABILITY

Lead contact

Further information and requests for resources and reagents should be directed to and will be fulfilled by the lead contact, Timm Maier (timm.maier@unibas.ch).

Materials availability

Plasmids used for NF1 expression are available upon request.

Data and code availability

- All maps and models will be made available on the Electron Microscopy Database (EMDB) and the Protein Databank (PDB) with accession codes EMD-14218, EMD-14219, and PDB ID 7R03, and 7R04.
- This paper does not report original code.
- Any additional information required to reanalyze the data reported in this paper is available from the lead contact upon request.

EXPERIMENTAL MODEL AND SUBJECT DETAILS

All recombinant proteins were produced in either SF21 insect cells grown in SFM4 medium (Cytiva) at 27°C, or BL21 (DE3) E. Coli cells grown in Luria Broth at 37°C. Cloning was performed in NEB 10-beta E. coli cells and insect cell expression plasmids were generated in DH10Multibac cells.

METHOD DETAILS

Construct for recombinant expression of neurofibromin

A synthetic human *NF1* gene (synNF1) codon optimized for expression in *Spodoptera frugiperda* was designed with an N-terminal 2xStrep tag sequence followed by a tobacco etch virus (TEV) protease recognition site in order to cleave the tag after purification. The modified *synNF1* gene was chemically synthesized by GeneArt AG, Life Technologies and was inserted into the multiple cloning site of the acceptor vector pACEBac1, where it is flanked by Tn7 13 transposition elements.

The Cys-Cys mutant is carrying the following mutations: L1520C, Y1524C, T2133C, and E2134C. Disease-causing (i.e. Neurofibromatosis type I causing) mutations were identified from two databases of genetic mutations: the Online Mendelian Inheritance in Man (OMIM) and the Human Gene Mutation Database (HGMD) (Amberger et al., 2015; Stenson et al., 2003). All other mutations made to neurofibromin are indicated in the main text.

Generation of recombinant bacmid DNA was performed by transforming *E. coli* DH10Multibac with pACEBac1 *synNF1* allowing insertion of the expression construct into the baculoviral DNA via Tn7 transposition. Recombinant bacmid DNA was isolated and used to transfect *Spodoptera frugiperda* (Sf21). cells which were cultivated in SF-900 III SFM medium at 100 rpm and 27°C to obtain the initial recombinant viruses.

Protein expression and purification for structural analysis

The initial recombinant baculoviruses were amplified and used for induction of neurofibromin expression by infecting Sf21 cells at a density of 0.5 – 1.0 x 10^6 cells/ml with a MOI (multiplicity of infection) > 1. After 72 hours of infection, cells were collected by centrifugation, washed in PBS and cell pellets were frozen in liquid nitrogen and stored at -80°C.

The cell pellet was resuspended in lysis buffer (20 mM HEPES pH 8.0, 300 mM NaCl, 10% glycerol, 5 mM TCEP) and flash frozen in liquid nitrogen. After thawing the cells, the lysate was supplemented with protease inhibitor cocktail (cOmplete™, EDTA-free, Roche) and cleared by centrifugation at 25,000 x g for 45 min at 4°C. Soluble fraction was collected and diluted 1:5 with lysis buffer followed by filtration through a 0.45 μm nitrocellulose membrane. The filtrated soluble fraction was loaded to a Strep Tactin Superflow Plus column (Qiagen) equilibrated in lysis buffer. The column was washed with 3 column volumes (CV) of lysis buffer and bound protein was eluted in lysis buffer supplemented with 5 mM d-Desthiobiotin. Fractions containing neurofibromin were collected, and the Strep tag was cleaved by 10 - 20 μg TEV protease (EMBL Heidelberg) pro ml eluate during dialysis using 3.5 kDa cut-off dialysis cassette (Thermo Scientific) against 2 L dialysis buffer (20 mM HEPES pH 8.0, 300 mM NaCl, 3 mM DTT) over night at 4°C. Neurofibromin was further purified by size exclusion chromatography (SEC) using a Superose 6 prep column 16/70 (GE Healthcare) equilibrated in 20 mM HEPES pH 8.0, 300 mM NaCl, 5 mM TCEP. The fractions containing the dimeric neurofibromin were pooled, concentrated using a 100 kDa cut-off concentrator (Vivaspin, Sartorius) and flash frozen in liquid nitrogen.

Protein production for activity assays

The coding sequence (codon-optimized) for the neurofibromin constructs were cloned into a baculovirus transfection vector (pACEBac2) fused to an N-terminal His10-myc-FLAG tag. This plasmid was transfected into Sf21 cells grown in HyClone medium (GE) using FuGENE (Promega). 4 days after transfection, the supernatant from the cells were collected and used to infect 50 mL of Sf21 in suspension culture in a 1:25 v:v ratio. The supernatant from that infection was then used to infect 500 mL of Sf21, which were then harvested via centrifugation at 1000 x g, after 3 more days of infection. The cells were resuspended in lysis buffer (20 mM HEPES pH 7.4, 500 mM NaCl, 0.1% NP40 and a cocktail of protease inhibitors including Pepstatin A, PMSF, E64, Bestatin, Phosphoramidon and Phenanthroline). Cells were lysed using a Dounce homogenizer and the lysate was cleared by centrifugation at 100,000 x g.

The lysate was applied to between 1 and 10mL of Anti-DYKDDDDK (FLAG) resin (Genscript). After 90 min of incubation at 4°C, the beads were washed with 20 volumes of lysis buffer and bound proteins were eluted with 3 volumes of elution buffer (20mM HEPES pH 7.4, 500 mM NaCl, 0.1 mg/mL DYKDDDDK peptide). The eluate was either concentrated and further purified over Superose 6 chromatography column equilibrated in SEC buffer (20 mM HEPES pH 7.4, 200 mM NaCl) or exchanged into SEC buffer, concentrated and snap frozen. While initially ten clinical mutants were targeted, one mutant, L844F, which is located in the helices below the GRD in the closed conformation, was not expressed and could therefore not be purified.

For isolation of the GAP related domain (GRD, 1191-1528) and the GRD-Sec14PH segment (1198-1830), the lysate was supplemented with 30 mM Imidazole and applied to a HisTrap Fast Flow Column (GE). The flow through was reloaded once and the column was washed with lysis buffer complemented with 30 mM Imidazole and the protein was eluted with elution buffer (20 mM HEPES pH 7.4, 500 mM NaCl, 200 mM Imidazole). The protein was then mixed in a 1:40 molar ratio with TEV protease and dialyzed overnight against Size Exclusion Chromatography (SEC) buffer (20 mM HEPES pH 7.4, 150 mM NaCl, 1 mM $MgCl_2$, 1 mM TCEP) supplemented with 30 mM Imidazole. After dialysis, the protein was passed once over a HisTrap column, concentrated using an Amicon concentrator, and injected on a Superdex 75 chromatography column equilibrated in SEC buffer. All fractions containing protein were pooled, concentrated to 7 mg/mL, frozen in liquid nitrogen and stored at -80°C until further use.

The coding sequence for the RasGEF domain of Sos1 (563-1049), obtained from I.M.A.G.E. was cloned into a bacterial expression vector (pET10) fused to an N-terminal His6 tag. BL21 (DE3) cells were transformed with the plasmid and grown to OD = 1.0 at 37°C in 2xYT medium, at which point they were shifted to 18°C, and expression was induced with 0.5 mM IPTG. The cells were then harvested by centrifugation at 3000 x g, resuspended in lysis buffer as above, supplemented with 0.01 mg/mL DNase and lysozyme, and lysed by sonication. The protein purification proceeded as described above. The protein was concentrated to 3 mg/mL, frozen and stored at -80°C.

HRas (1-161) and Spred1-EVH1 were produced as described in Dunzendorfer-Matt et al., 2016.

Cryo-EM sample preparation and collection

Cryo-EM grids of neurofibromin were prepared on a Leica EM GP plunge-freezer at 20°C and 100% humidity. Quantifoil R2/1 200 mesh were glow discharged 30 seconds at 50 mA. For the neurofibromin apo grids, the protein was diluted to 0.3 mg/mL in a buffer containing 20mM Tris 200 mM NaCl and 1 mM TCEP just prior to grid preparation. 4 μL of solution was then applied onto the glow-discharged grids and blotted 3 sec before plunge-freezer into liquid ethane (-180°C). For the neurofibromin:GTPγS:HRas grids, the protein was diluted to 0.3 mg/mL followed by addition of a 10-fold molar excess of HRas:GMPPNP (approximately 0.23 mg/mL) and 10 mM of GTPγS. For all neurofibromin:nucleotide grids, neurofibromin was diluted to 0.3 mg/mL with 10 mM of either GTPγS

or ATP. Cryo-EM data was collected on a Titan Krios (FEI) mounted with a K2 summit detector (Gatan Inc.). Nominal magnification was 130,000X corresponding to a pixel size of 1.058 Å/pix. For the first neurofibromin data set, 40-frame movies were collected in counting mode with 10 seconds of total exposure, corresponding to a total electron dose of 60 e/Å^2. For the second neurofibromin dataset, 32-frame movies were collected with 8 seconds of total exposure corresponding to a total electron dose of 50 e-/Å^2. Both neurofibromin:GTPγS:HRas datasets were collected as 40-frame movies in counting mode with 10 seconds of total exposure, corresponding to a total electron dose of 50 e/Å^2. Neurofibromin:nucleotide datasets were collected in 30-frame movies for 3 sec on a TFS Glacios mounted with a K3 detector, corresponding to a total electron dose of 50 e/Å^2. The nominal magnification was 36,000X corresponding to a pixel size of 1.113 Å/pix.

Cryo-EM data processing

For the neurofibromin-apo datasets, all movies were imported directly into cryoSPARC v2 (Punjani et al., 2017) (Figure S2). Movies were initially aligned using patch motion correction and CTF was determined using Patch CTF determination. Manual picking on 100 micrographs was initially used to generate picking templates. Template picked was then performed and the corresponding particles were extracted with a box size of 560 pixels (Fourier-cropped to 280). After several rounds of 2D classification, the best particles were pooled together, for a total of more than 700k particles, and subjected to ab initio reconstruction and 3D refinement. The particles the underwent 3D classification with 3 classes using the Heterogeneous refinement function cryoSPARC. The particles which formed the best class, which showed clear density for both lobes of the molecule, were then locally aligned using local motion correction and extracting the full box size. Those locally aligned particles were then used for NU-refinement (Punjani et al., 2020), yielding a 3.7 Å reconstruction. Using local refinement and masks covering either side of the molecule, we obtained the two maps with improved resolution of 3.6 and 3.7 Å respectively. A third locally refined map was obtained by masking the central region of the molecule, improving the resolution to 3.6 Å. All masks used for processing were generating using Chimera (Pettersen et al., 2004). The neurofibromin:GTPγS:HRas data was initially analyzed in a similar fashion. Classification revealed multiple functional conformation included an ''open conformation'' and a semi-open conformation with density for one of the GRD in the closed conformation while the other GRD was flexible and not well resolved. These conformations were refined separately yielding reconstructions with resolutions of 3.7 and 3.5 Å, respectively. The open conformation was then further analyzed using local refinement in order to improve the resolution of the nucleotide binding site. From this, we generated two additional locally refined maps at resolution of 3.5 to 3.6 Å.

The neurofibromin + ATP/ GTPγS datasets were analyzed similarly in cryoSPARC. Low to medium-resolution reconstruction showed that no particles were in the occluded conformation. However, few particles seemed to be in the clear ''open conformation'' with broken asymmetry as in the Ras containing sample, suggesting that the nucleotide release the auto-inhibitory contact but the presence of Ras may stabilize the GRD into its central location adjacent the CDM.

Structural modeling and visualization

All structural modeling was done in Coot (Emsley and Cowtan, 2004) using all maps simultaneously. The crystal structure for the GRD (PDB: 6V65) and the Sec14-PH domain (PDB: 2E2X) (Welti et al., 2007) was initial docked in the cryo-EM map using Chimera (Pettersen et al., 2004). The placement of these two domains was subsequently adjusted in Coot. For the rest of the model, ideal alpha helices were placed in the EM map and their register was determined based on the side chain density and location relative to the GRD and Sec14-PH domains. This allowed us to trace the entire backbone of the protein, using large sidechains as hallmarks. The model was validated using the AlphaFold 2.0 prediction as comparison (Figure S4), which shows good agreement (Jumper et al., 2021). Once the modeling in Coot was completed, the modeled was real-space refined in PHENIX (Adams et al., 2010) against a composite map of all the different locally refined cryo-EM reconstructions, using secondary structure restraints. The closed confirmation model was then used as the basis for modeling of subsequent conformations, with adjustments as needed. The GRD and Sec14PH showed strong density for chain A, which facilitated docking and modeling, but exhibited markedly weaker density for chain B, indicating flexibility. The two domains of chain B were nevertheless placed with the best possible fit, but this reconstruction likely represents an average of an ensemble of conformation for these 2 domains. The model for the open conformation was then refined as before.

HPLC-based Ras GAP assay

Nucleotide free HRas was purified by dialyzing HRas-GDP against 20 mM HEPES pH=7.4, 100 mM NaCl and 20 mM EDTA, overnight at 4°C. The remaining protein was separated from the nucleotide by injecting it on a Mono Q 1 mL ion exchange column (GE) and eluted by running a 100 mM to 1 M NaCl gradient (with 20 mM HEPES pH=7.4).

Ras GAP activity for neurofibromin variants was measured by mixing 10 μM nucleotide free HRas, 1 mM GTP, 2 mM $MgCl_2$, 1 μM Sos1GEF with either 0.1 or 1 μM neurofibromin variant, in 20 mM HEPES and 150 mM NaCl, in triplicate (or sextuplicate for wild type neurofibromin). Protein concentrations were determined via absorbance measurements at 280 nm on a Nanodrop 2000. The reaction mixtures were shaken (600rpm) at room temperature and samples were snap frozen at time points 0 and 30 min. The samples were then incubated 2 min at 98°C before adding 4 volumes of RPC-A buffer (5 mM TBAC, 10 mM Na/KPO_4 pH=7) and spinning down 5 min to pellet the protein. The supernatants were transferred to a clean tube and half of the solution was injected on a Kinetex EVO C18 (Phenomenex), before eluting the nucleotides with a 3-100% gradient of RPC-B buffer (75% Acetonitrile, 5 mM TBAC,

10 mM Na/KPO_4). GTP consumption was calculated by integrating the GDP and GTP peaks from each sample and calculating the relative amount of GDP accumulation.

To measure ATP activation, the same assay was performed with the following adjusted concentrations: 5 μM nucleotide free HRas, 200 μM GTP, 3 mM $MgCl_2$, 0.5 μM Sos1GEF, 0.02 μM neurofibromin variant and either 0 or 2 mM ATP. 100 μM of cAMP was also added to the reaction as an internal standard. The samples were otherwise processed identically.

SEC-MALS

SEC-MALS measurements for neurofibromin were performed at a sample loading concentration of 0.5 mg/mL at 25°C in 20 mM HEPES pH=7.4, 200 mM NaCl using a GE Healthcare Superose 6 10/300 Increase column on an Agilent 1260 HPLC. Elution was monitored using an Agilent multi-wavelength absorbance detector (data collected at 280 and 254 nm), a Wyatt Heleos II 8+ multiangle light scattering detector and a Wyatt Optilab rEX differential refractive index detector. The column was equilibrated overnight in the running buffer to obtain stable baseline signals from the detectors before data collection. Inter-detector delay volumes, band broadening corrections, and light-scattering detector normalization were calibrated using an injection of 2 mg/ml BSA solution (ThermoPierce) and standard protocols in ASTRA 7. Weight-averaged molar mass (Mw), RMS radius, elution concentration, and mass distributions of the samples were calculated using ASTRA 7 software (Wyatt Technology).

Mass spectrometry analysis

To determine the phosphorylation state of neurofibromin, 5 μg of neurofibromin was diluted in 0.1 M ammonium carbonate and digested overnight with either 0.5 μg of trypsin or 1 μg of Glu-C proteases. After digestion, the solution was acidified to a pH of less than 2 with 20% TFA and applied to a BioPureSPN MACRO™ SPE C18 cartridge pre-equilibrated with 0.1% TFA. After washing the cartridge in 5% Acetonitrile 0.1% TFA buffer, the peptides were eluted with a 50% Acetonitrile 0.1%TFA solution. The eluate was dried in a vacuum concentrator and the peptides were finally resuspended in 30 μL of LC buffer A (0.15% Formic acid, 2% acetonitrile). 1 pmol of solution was analyzed with a Q Exactive™ Plus Hybrid Quadrupole-Orbitrap™ fitted with an EASY-nLC 1000. Peptides were resolved using a EasySpray RP-HPLC column (75μm × 25cm) at a flow rate of 0.2 μLmin-1. A linear gradient ranging from 5% buffer B to 45% buffer B over 60 minutes was used for peptide separation. Buffer A was 0.1% formic acid in water and buffer B was 80% acetonitrile, 0.1% formic acid in water. The mass spectrometer was operated in DDA mode with a total cycle time of approximately 1 s. Each MS1 scan was followed by high-collision-dissociation (HCD) of the 20 most abundant precursor ions with dynamic exclusion set to 5 seconds. For MS1, 3e6 ions were accumulated in the Orbitrap over a maximum time of 25 msand scanned at a resolution of 70,000 FWHM (at 200 m/z). MS2 scans were acquired at a target setting of 1e5 ions, maximum accumulation time of 110 ms and a resolution of 17,500 FWHM (at 200 m/z). Singly charged ions, ions with charge state $\geq$ 6 and ions with unassigned charge state were excluded from triggering MS2 events. The normalized collision energy was set to 27%, the mass isolation window was set to 1.4 m/z and one microscan was acquired for each spectrum. The resulting spectra were searched against the neurofibromin sequence and the Sf21 proteome. The raw files were analyzed using FragPipe (v17.1) using MSFragger (v.3.4) and the "Labile_phospho" workflow with default DDA setting including MS1 Quant to obtain PTM site probabilities. The database search results were imported into Scaffold (v.5.1.0) and filtered to 1% FDR on protein and peptide level using build in Percolator algorithm.

Isothermal titration calorimetry

Affinity of neurofibromin to various nucleotides was measured by isothermal titration calorimetry on a MicroCal iTC200, using the minimal neurofibromin construct GRD-Sec14PH. The nucleotides were dissolved to 50 mM in 20 mM HEPES pH=7.4, 150 mM NaCl, and 50 mM $MgCl_2$, and the pH was adjusted to 7.4. The protein was placed in the ITC cell at 20 mg/mL. The nucleotide was injected via in one 1 x 0.4 μL and 18 x 2 μL injections. A blank run was performed with buffer in the cell and the same nucleotide solution in the syringe for data subtraction. This step was essential due to the very high heats of dilution caused by the high nucleotide concentration in the syringe. The data were analyzed using the online version of Affinimeter. Integrated heats for each injection of the appropriate blank run were subtracted from those of each experimental run to yield a binding isotherm. The binding isotherms from replicate measurements of the same nucleotide binding to GRD-Sec14PH were globally fitted to a 1:1 binding model without applying concentration corrections, sharing the value of the association constant ($1/K_D$) and enthalpy of binding between all datasets.

Thermal stability measurement

Thermal stability of neurofibromin variants was assessed by differential scanning fluorimetry. Protein solution at a concentration of 0.2-0.3 mg/mL was loaded in capillaries and measured in a Prometheus (Nanotemper). Thermal denaturation curves were measured obtained by monitoring measuring intrinsic fluorescence with excitation at 280 nm and emission at 330 and 350 nm, and apparent absorbance of excitation light due to fluorescence and light scattering, during a continuous temperature ramp from 20 to 95°C with a rate of 1°C/min gradient.

QUANTIFICATION AND STATISTICAL ANALYSIS

Statistics for the cryo-EM structures of neurofibromin were generated by PHENIX after refinement.

Statistical significance of the GAP activity assays was determined by Student's t-test in Prism 9 (Graph Pad).